Journal of The Electrochemical Society, **150** (2) G127-G139 (2003)
0013-4651/2003/150(2)/G127/13/$7.00 © The Electrochemical Society, Inc.

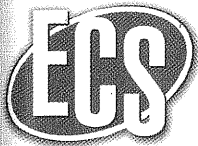

An Investigation of Particle Dynamics in a Rotating Disk Chemical Vapor Deposition Reactor

D. M. Kremer,[a] R. W. Davis,[b,z] E. F. Moore,[b] J. E. Maslar,[b] D. R. Burgess, Jr.,[b] and S. H. Ehrman[a]

[a]*Department of Chemical Engineering, University of Maryland, College Park, Maryland 20742-2111, USA*
[b]*Chemical Science and Technology Laboratory, National Institute of Standards and Technology, Gaithersburg, Maryland 20899-8360, USA*

This paper describes a numerical model for the nucleation, growth, and transport of gas-phase particles formed during the chemical vapor deposition (CVD) of epitaxial silicon from silane. These particles can lower the deposition rate by consuming precursor, and contaminate the growing film via diffusion to the surface. This model has been constructed for use with the Sandia SPIN code, which contains a solver for the reacting flow and heat transfer in a vertical, rotating disk CVD reactor. A detailed gas-phase chemical kinetic mechanism for the thermal decomposition of silane was developed to simulate formation of small silicon clusters and the depletion of reactive intermediates through condensation. The particle model uses a moment transport formulation to examine the effects of total reactor pressure, temperature, rotation rate, inlet gas composition, and rate of particle growth via condensation on the characteristics of the particle population. Numerical results are presented in terms of the integral moments of the particle distribution which correspond physically to the particle number concentration, average particle diameter, and particle light scattering intensity. *In situ* validation experiments have been performed in an optically accessible reactor under conditions typical of silicon CVD. The rate of particle growth via condensation, controlled numerically by a global condensation parameter (GCP), was found to control the characteristics of the particle population. The numerical results were found to compare favorably with experiment if this GCP was properly chosen.
© 2003 The Electrochemical Society. [DOI: 10.1149/1.1536180] All rights reserved.

Manuscript submitted January 16, 2002; revised manuscript received June 17, 2002. Available electronically January 9, 2003.

Thermal chemical vapor deposition (CVD) is a process in which a gaseous mixture of reactive precursors flows over a heated substrate upon which a solid film deposits. The deposition of silicon thin films via CVD has been the topic of extensive research efforts.[1,2] Stringent film quality tolerances imposed by the microelectronics industry have led researchers to investigate many features of the CVD process in order to gain an understanding of how fundamental physical and chemical phenomena impact film quality. A thorough description of CVD must incorporate numerous physical and chemical processes. These processes include the formation of film growth precursors through both homogeneous and heterogeneous chemical reaction. Additionally, convective transport involves complex flow fields coupled with both heat and mass transfer. Finally, homogeneous particle nucleation, growth, and transport must also be considered because the formation of particles can lower the deposition rate by consuming the precursor and contaminate the growing film via diffusion to the surface.

In this paper we describe a collaborative numerical and experimental research effort to investigate the gas-phase nucleated particles formed during the CVD of epitaxial silicon from a common gaseous precursor, silane. It has long been observed that SiH_4 will easily decompose under typical CVD conditions.[3-5] Several studies have focused on the gas-phase decomposition pyrolysis of SiH_4. Coltrin *et al.*[6] produced a limited 20 step pyrolysis mechanism for SiH_4 by performing a sensitivity analysis on a large system of possible decomposition reactions. Early attempts to describe the gas-phase SiH_4 decomposition chemistry made no attempt to account for particle formation. However, Eversteijn[7] clearly observed the formation of a visible layer of particles while performing experiments using a mixture of SiH_4 and hydrogen. Only recently have researchers begun to develop gas-phase pyrolysis mechanisms which account for this phenomenon. Swihart and Girshick[8] presented an extensive mechanism for the gas-phase pyrolysis of SiH_4 which described the formation of hydrogenated silicon clusters. Such mechanisms are necessary for a thorough description of the gas-phase decomposition chemistry.

The numerical modeling of CVD reactors has been an active area of research. Past research has assimilated kinetic models with transport models in two broadly defined categories. Some researchers have focused on the complex flow fields and heat transfer which are a characteristic of the CVD process.[9-14] The goal of these research efforts was to identify reactor operating regimes which resulted in well-defined fluid flow, free from buoyant instabilities near the deposition surface. Operation of the reactor within these regimes would offer a uniform flux of film precursors to the deposition surface and thus result in well-controlled film deposition. Davis *et al.*[15] expanded this concept by combining a two-dimensional flow and heat-transfer model with a description of particle dynamics in a vertical, rotating disk CVD reactor. However, the particles were injected into the flow field at arbitrary locations and were not subject to any growth processes. Other research has coupled simplified flow and heat transfer models with complex gas-phase and surface chemical reaction mechanisms to more completely describe the deposition process itself.[6,16-19] Neither modeling approach has successfully described the nucleation, growth, and transport of gas-phase generated particles. Recently, several studies have been conducted which attempt to rectify this deficiency. Whitby and Hoshino[20] coupled a moment transport aerosol model to a two-dimensional flow, chemistry, and heat transfer model to describe particle formation during the deposition of SiO_2 in a horizontal CVD reactor. Girshick *et al.*[21] employed a detailed clustering mechanism to describe the formation of silicon hydride particles during silane pyrolysis in a vertical stagnation reactor.

The current research effort described here utilizes two models (one-dimensional and two-dimensional axisymmetric) to simulate the flow and heat transfer in a vertical, rotating disk CVD reactor. The nucleation, growth, and transport of particles is simulated in the one-dimensional model via a moment transport formulation for the simulation of aerosol populations following Whitby *et al.*[22] To the authors' knowledge, this model offers the most complete description to date of the aerosol population found during the CVD of silicon from SiH_4. The two-dimensional axisymmetric model includes only flow and heat transfer, and is utilized in order to obtain more realistic temperature profiles for better comparison with experimental results. Model outputs are compared directly with *in situ* experimental data obtained in an optically accessible reactor apparatus. An empirical parameter in the one-dimensional model which controls the rate of condensation is shown to control the characteristics of the

[z] E-mail: rwdavis@nist.gov

aerosol population. Proper selection of this parameter is demonstrated to produce excellent agreement between numerical and experimental results.

Numerical Modeling

Flow and heat transfer models.—There were two numerical models employed during the course of this investigation. The most detailed model was based on the Sandia SPIN code[23] which was developed to solve for the reacting flow in a vertical, rotating disk CVD reactor. The formulation employed by the SPIN code is based on a modified form of the von Karman similarity transformation that reduces the central region of the reactor to a one-dimensional domain above an infinite radius disk.[16] This approach allows the transport equations, energy equation, and chemical species equations to be solved via a series of ordinary differential equations which depend solely on the axial coordinate. The SPIN code uses two constituent solvers to simulate the gas-phase and surface chemical reactions, CHEMKIN[24] and SURFACE CHEMKIN,[25] respectively, while variable transport properties are determined from TRANSPORT.[26] It has been demonstrated by Ho *et al.*[3] that, under appropriate reactor operating conditions, the SPIN model is capable of describing the CVD of silicon in a vertical, rotating disk reactor. However, it has been reported that the accuracy of the SPIN solution begins to degrade as the boundary layer thickness approaches the radius of the susceptor, as is known to occur at very low reactor pressures.[14] Use of the SPIN code under these conditions can lead to solutions which exhibit nonphysical oscillations and slope discontinuities at the inflow boundary.[21,27,28]

The one-dimensional nature of the SPIN code limits its applicability to a region near the central portion of the reactor. Thus, the one-dimensional model fails to account for several salient features of the reactor such as the finite radius of the rotating disk and the presence of the reactor walls.[29] Additionally, the modified form of the von Karman transformation is mathematically incapable of simulating the buoyancy induced recirculating flow fields known to sometimes occur in vertical, rotating disk CVD reactors.[10,12] For these reasons, a more descriptive model of the flow field and heat transfer has been constructed based on the work of Davis *et al.*[15] This model solves the full axisymmetric Navier-Stokes and energy equations on a variably spaced staggered mesh, and offers a much more complete description of the reactor flow field and heat transfer than is possible via SPIN. The axisymmetric model is capable of simulating flow fields in which buoyant recirculation instabilities are present. Gas-phase chemical reactions were not considered in the two-dimensional model due to the low concentration of SiH_4 in the carrier gas. Two-dimensional simulations were used to verify that, given a set of reactor operating conditions, the flow field and heat transfer could reasonably be described by the one-dimensional SPIN model. Additionally, two-dimensional centerline temperature profiles were used as inputs to the SPIN model in an attempt to better simulate the actual experimental reactor environment.

Gas-phase chemical reaction mechanism.—The reactions comprising the chemical kinetic mechanism for the decomposition of silane and subsequent chemistry, Table I, were based on the extensive mechanism development work for this system by Coltrin *et al.*[3,6,16,17] Several reactions for SiH_2 and Si were taken from work by Mick *et al.*[30,31] and Martin *et al.*[32] A number of additional gas-phase reactions, which may be relevant at higher temperatures and silane concentrations, were added to this reactions set. The rate expressions for these reactions were estimated by analogy to similar reactions. Table II presents the low pressure kinetic parameters and the Troe fall-off parameters[33] for the collision-activated reactions. The overall gas-phase chemistry is a series of direct and indirect dehydrogenation steps in the direction of thermodynamic equilibrium and the formation of solid silicon as both deposition on the substrate surface and the formation of particles. A short summary of the overall chemistry is that the first, and largely rate-determining, step is an initial dehydrogenation of silane (Table I, Reaction 1), and establishment of a partial equilibrium among the silanes (SiH_4, Si_2H_6, etc.) and disilene ($SiH_2 = SiH_2$) driven by the steady-state concentrations of the reactive silylenes SiH_2 and SiH_3SiH. The second step is dehydrogenation of disilene to form Si_2H_2 and establishment of a partial equilibrium among the small silicon hydrides. It is these species (Si_2H_2 and the small silicon hydrides) that are largely responsible for the formation of solid silicon (both on the surface and particles).

The gas-phase kinetic mechanism in use here to simulate the formation of silicon clusters is an extension of a mechanism which has been used successfully to model the gas-phase silicon atom profiles encountered during the CVD of silicon from silane in a similar reactor operating at comparable conditions.[3] Using *in situ* experimental studies performed under very similar conditions to the present research effort, these researchers revealed that highly nonequilibium concentrations of gas-phase silicon atoms exist in the thermal boundary layer close to the susceptor surface.[3,34] Additionally, other researchers have examined the silicon particles formed during the thermal decomposition of silane, and found them to be almost completely dehydrogenated under conditions similar to the current research effort.[35,36] It should be noted that the clustering mechanism employed here is simply a tractable representation of what other researchers[8,21] have postulated to be a much more complicated chemical process involving various species and reactions pathways not considered in this work. However, to the authors' knowledge, the precise kinetic mechanism for homogeneous silane to silicon conversion has not been reported. For this reason, a simple set of clustering reactions was added to the gas-phase reaction set which involve the reaction of Si_n clusters with other clusters (Table I, Reaction 22) and with two reactive intermediates, SiH_2 and Si_2H_2, which are present in relatively high concentrations, see Fig. 1. The clustering reactions were terminated at Si_6 with larger clusters considered as monomer sources, denoted Si(P) for particle formation (Table I, Reaction 32). Procedurally, in the chemical mechanism, this was accomplished with reactions similar to $Si_4 + Si_2H_2 \rightarrow Si_6 + H_2$ and $Si_5 + Si_2H_2 \rightarrow 7Si(P) + H_2$. Thus, any reaction that produced a cluster with more than six Si atoms was considered to form multiple nSi(P) rather than a single cluster Si_n. The rate of formation of Si(P) was used as the source term for the rate of nucleation by the aerosol model.

A single species, Si_2H_2, was chosen to act as the condensable species because it is reactive and present in relatively high concentrations (see Fig. 1). The rate of condensation was computed from the concentration of the condensable species and the surface area of the particles derived from the moments of the particle distribution. In the gas-phase chemical mechanism, Si(C) was used to track the amount of silicon which had condensed through Reaction 33, Table I. Undoubtedly, species other than Si_2H_2 will react with the silicon particles, but in the absence of any prior knowledge of the relative rates, the use of a single condensable species is all that is reasonable. The rate of condensation could also depend on additional factors such as particle size and structure, and strongly upon the amount of hydrogen on the surface of the particles (a hydrogen surface would be relatively unreactive, while a bare silicon surface would be very reactive). Again, in the absence of prior knowledge, the use of a spatially invariant global condensation parameter (GCP) with a value selected to best match experimental observables is all that is warranted. As detailed above, several assumptions and simplifications have been made during the construction of the kinetic mechanism used for this investigation. For these reasons, this research effort focuses primarily on elucidating trends in particle formation during the CVD of silicon from silane. Quantitative comparison based on the aerosol model output has been avoided wherever possible.

Aerosol model.—The numerical modeling of aerosol populations is relevant to many diverse applications such as combustion and atmospheric air quality research. As a result, many techniques have

Table I. Gas-phase reaction mechanism. The high pressure forward rate constants are expressed in the form $k_{inf} = A\ T^b \exp(-E/RT)$.

No.	Reactions	*A* (cm³, mol, s)	*b*	*E* (kJ/mol)	Ref.
	Unimolecular decompositions				
1	$SiH_4(+M) = SiH_2 + H_2$	3.12×10^{9}	1.7	228.9	3
2	$Si_2H_6(+M) = SiH_4 + SiH_2$	1.81×10^{10}	1.7	210.0	3
3	$Si_2H_6(+M) = H_3Si_2H + H_2$	9.09×10^{9}	1.8	226.8	3
4	$Si_3H_8(+M) = Si_2H_6 + SiH_2$	6.97×10^{12}	1.0	220.4	3
5	$Si_3H_8(+M) = H_3Si_2H + SiH_4$	3.73×10^{12}	1.0	212.8	3
6	$SiH_2 + M \rightarrow Si + H_2 + M$	9.90×10^{20}	−1.8	160.0	30
7	$SiH_4 + Si = H_3Si_2H$	1.00×10^{12}	0.0	20.9	Est.
8	$H_2Si_2H_2 = Si_2H_2 + H_2$	3.16×10^{14}	0.0	221.8	16
9	$H_2Si_2H_2 = SiH_2 + SiH_2$	1.00×10^{16}	0.0	246.9	17
10	$SiH_2 + Si = Si_2H_2$	7.24×10^{12}	0.0	8.4	6
11	$Si_2 + H_2 = Si_2H_2$	1.54×10^{13}	0.0	8.4	6
	Isomerizations				
12	$H_3Si_2H = H_2Si_2H_2$	2.54×10^{13}	−0.2	22.5	3
	Activated decompositions				
13	$H_3Si_2H + H_2 = SiH_4 + SiH_2$	9.41×10^{13}	0.0	17.1	3
14	$SiH_4 + H_3Si_2H = Si_2H_6 + SiH_2$	1.73×10^{14}	0.4	37.2	3
15	$SiH_2 + SiH_2 = Si_2H_2 + H_2$	6.50×10^{14}	0.0	0.0	31
16	$Si + SiH_4 = Si_2H_2 + H_2$	1.50×10^{14}	0.0	30.5	30
17	$Si + SiH_2 = Si_2 + H_2$	1.50×10^{14}	0.0	0.0	30
18	$Si_2H_6 + Si = SiH_2 + H_3Si_2H$	1.30×10^{15}	0.0	52.7	3
	Si_m clusters				
19	$Si + Si + M = Si_2 + M$	2.47×10^{16}	0.0	4.9	32
20	$Si_2 + Si + M = Si_3 + M$	2.50×10^{16}	0.0	5.0	Est.
21	$Si_3 + Si = Si_2 + Si_2$	2.06×10^{12}	0.0	100.8	6
22	$Si_n + Si_m \rightarrow Si_{n+m}$	1.00×10^{12}	0.0	0.0	Est.
	$Si_n + SiH_2$ clusters				
23	$Si_2 + SiH_2 = Si_3 + H_2$	3.55×10^{11}	0.0	8.4	16
24	$Si_2 + SiH_2 = Si + Si_2H_2$	1.00×10^{12}	0.0	0.0	Est.
25	$Si_n + SiH_2 \rightarrow Si_{n+1} + H_2$	1.00×10^{12}	0.0	0.0	Est.
	$Si_n + Si_2H_2$ clusters				
26	$Si_3 + H_2 = Si + Si_2H_2$	9.79×10^{12}	0.0	197.5	16
27	$Si_3 + SiH_2 = Si_2 + Si_2H_2$	1.43×10^{11}	0.0	78.7	6
28	$Si_n + Si_2H_2 \rightarrow Si_{n+2} + H_2$	1.00×10^{12}	0.0	20.9	Est.
29	$Si_n + Si_2H_2 \rightarrow Si_{n+1} + SiH_2$	5.00×10^{11}	0.0	20.9	Est.
	Si_2H_2 clusters				
30	$Si_2H_2 + SiH_2 \rightarrow Si_3 + 2H_2$	5.00×10^{11}	0.0	20.9	Est.
31	$Si_2H_2 + Si_2H_2 \rightarrow Si_4 + 2H_2$	5.00×10^{11}	0.0	41.8	Est.
	Si_n particles				
32	$Si_n \rightarrow (n)Si(P)$	1.0			$n > 6$
33	$Si_2H_2 + Si(s) \rightarrow 2Si(C) + Si(s) + H_2$	$0 < \alpha < 1$			

Table II. Low pressure kinetic parameters ($k_0 = A\ T^b \exp(-E/RT)$) and Troe fall-off parameters (a, T^{***}, T^{*}, T^{**}) for collision-activated reactions. The numbers correspond to reactions indicated in Table I.

	Low pressure kinetic parameters			Troe parameters[33,a]				
No.	*A* (cm³, mol, s)	*b*	*E* (kJ/mol)	*a*	T^{***}	T^{*}	T^{**}	Ref.
1	5.21×10^{29}	−3.54	240.8	−0.4984	888.3	209.4	2760	3
2	5.09×10^{53}	−10.37	234.4	4.375×10^{-5}	438.5	2726.0	438.2	3
3	1.94×10^{44}	−7.77	246.9	−0.1224	793.3	2400.0	11.39	3
4	1.73×10^{69}	−15.07	253.1	-3.47×10^{-5}	442.0	2412.0	128.3	3
5	4.36×10^{76}	−17.26	248.1	0.4157	365.3	3102.0	9.72	3

[a] Both SiH_4 and Si_2H_6 have four times enhanced third-body collision efficiency.

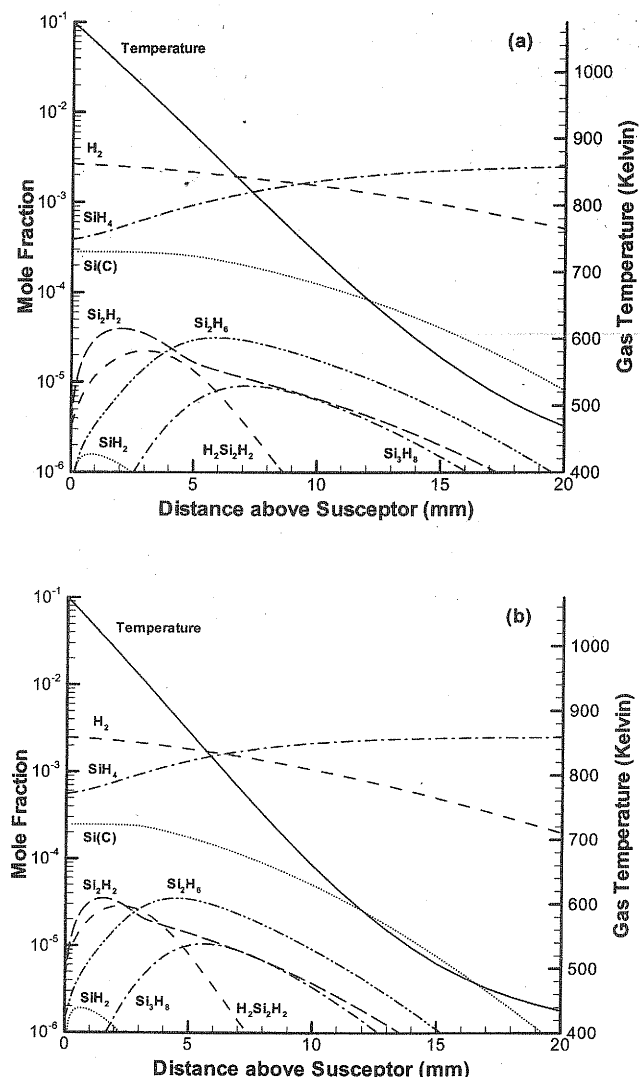

Figure 1. Species concentration profiles and gas-phase temperature profiles *vs.* axial distance above the susceptor. $T_{\text{susceptor}} = 1075$ K, $P_{\text{total}} = 26.7$ kPa (200 Torr), 0.25% SiH_4 in helium, and $U_\infty = 22$ cm/s. (a) $\omega = 500$ rpm, $\alpha = 0.03$, (b) $\omega = 1000$ rpm, $\alpha = 0.08$.

evolved to numerically simulate aerosol populations.[37] For the present research effort, a parametrized moment transport formulation has been chosen to simulate the aerosol population based on the work of Whitby *et al.*[22] While a parametrized model requires an *a priori* assumption as to the functional form of the aerosol distribution, it is able to capture many physical processes with reasonable computational effort.[22,37]

The moment transport aerosol dynamic model employed in this study is able to account for particle nucleation, transport, and growth due to coagulation and condensation. Each of these particle growth processes is occurring as the carrier gas flows through the reactor. Thus, the aerosol dynamics model must also consider several transport processes. The bulk of the aerosol population is moving with the carrier gas, so a primary means of particle transport is convection. However, particles can also be transported under the influence of concentration gradients (diffusion) or temperature gradients (thermophoresis). Gravity can also influence the motion of a particle. A representation of the growth and transport processes considered by the aerosol model is illustrated in Fig. 2.

A parametrized aerosol model must incorporate the effects of growth and transport processes on the behavior of the aerosol population. This is accomplished mathematically by representing the aerosol population as a continuous distribution function which specifies the number of particles as a function of their diameter. The moment transport formulation of Whitby *et al.*[22] assumes that the aerosol population can be adequately represented by a lognormal distribution function. A lognormal distribution function is utilized because of its wide applicability to a number of physical systems,[38] and can be represented by the following equation

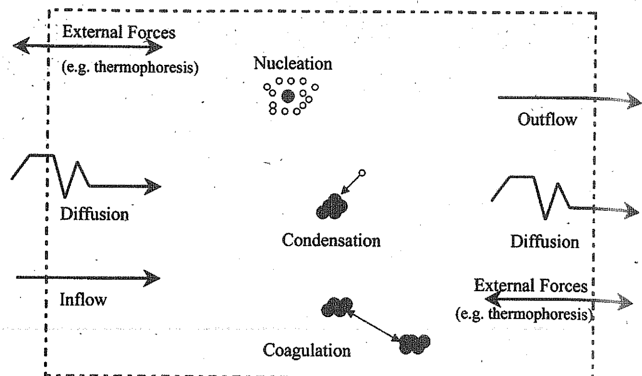

Figure 2. Particle growth and transport processes considered by the moment transport aerosol model.

$$n(\ln d_p) = \frac{N}{\sqrt{2\pi}\ln\sigma_g}\exp\left[-0.5\frac{(\ln d_p - \ln D_{gn})^2}{\ln^2\sigma_g}\right] \qquad [1]$$

where N is the total number concentration, d_p is the particle size, D_{gn} represents the geometric mean size of the number weighted lognormal distribution, and σ_g is the variance.[22] Because the distribution function is composed of multiple parameters, equations cannot be written which solve directly for the distribution. Significant simplification arises if the aerosol dynamics equations are written in terms of the integral moments of the distribution. Friedlander[39] defines the integral moments of the distribution as follows

$$M_k = \frac{1}{\rho}\int_0^\infty d_p^k n(d_p)d(d_p) \qquad [2]$$

where ρ is the gas density, n represents the lognormal distribution function, and k is an integer quantity. The effect of the growth and transport processes on the evolution of the integral moments of the distribution is represented by the moment dynamic equation expressed by Friedlander[39] as

$$\begin{aligned}\frac{\partial}{\partial t}\rho M_k = &-\underbrace{\nabla\cdot v\rho M_k}_{\text{Convection}} - \nabla\cdot\underbrace{\int_0^\infty d_p^k c(d_p)n(d_p)d(d_p)}_{\text{External Forces}}\\ &+\nabla\cdot\underbrace{\int_0^\infty d_p^k D(d_p)\nabla n(d_p)d(d_p)}_{\text{Diffusion}}\\ &+\underbrace{\frac{1}{2}\int_0^\infty\int_0^\infty d_{p12}^k\beta(d_{p1},d_{p2})n(d_{p1})n(d_{p2})d(d_{p1})d(d_{p2})}_{\text{Particle-particle coagulation source}}\\ &-\frac{1}{2}\int_0^\infty\int_0^\infty (d_{p1}^k\\ &+\underbrace{d_{p2}^k)\beta(d_{p1},d_{p2})n(d_{p1})n(d_{p2})d(d_{p1})d(d_{p2})}_{\text{Particle-particle coagulation sink}}\\ &+\underbrace{\int_0^\infty\frac{d(d_p^k)}{d(v_p)}\frac{\partial}{\partial t}(v_p)n(d_p)d(d_p)}_{\text{Condensation}} + \underbrace{\int_0^\infty d_p^k\dot{n}_s(d_p)d(d_p)}_{\text{Nucleation}}\end{aligned} \qquad [3]$$

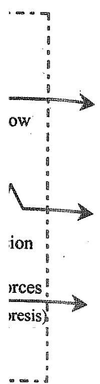

where v is the gas convection velocity, $\dot{n}_s$ is the production rate of particles of diameter d_p, $c(d_p)$ is the particle velocity due to external forces, d_{p12} is the diameter of the coagulated particle, $D(d_p)$ is the diffusion coefficient for particles of diameter d_p, v_p is the particle volume, and β is the coagulation coefficient.

Most aerosol models which employ the moment transport formulation use the same solution set consisting of the M_0 (particle number concentration), M_3 (particle volume fraction), and M_6 (particle light scattering intensity) integral moments. There are two reasons for the selection of these moments. Using this set of moments makes it possible to obtain a closed set of expressions in which all of the integrals in the moment dynamic equation can be written in terms of the other moments in the solution set. Additionally, other researchers[40,41] have derived approximate interpolation formulas for the complex coagulation integrals in the moment dynamic equation in terms of the other moments in this basis set.

The moment transport equation for the present one-dimensional configuration is represented by the following governing differential equation

$$\frac{\partial(\rho M_k)}{\partial t} + \frac{\partial[\rho(u + c_k)M_k]}{\partial z} = \frac{\partial}{\partial z}\left(\Gamma_k \frac{\partial M_k}{\partial z}\right) + S_k \quad [4]$$

where u is the convection velocity; c_k is the transport velocity of M_k due to gravity, drag, and thermophoresis; Γ_k is the diffusion coefficient of M_k, and S_k is the moment source term due to chemical production, coagulation, and condensation. The challenge in using the moment transport model is to express each of the terms in the governing equation in terms of the three moments which comprise the basis set. The temporal derivative in the governing equation approaches zero as the solution approaches steady state.

The modeling of each term is sufficiently complex that it will only be outlined here (see Whitby *et al.*[22] for details). The drag force acting on the particles is computed by assuming Stokes drag.[42] The two external forces considered by the aerosol model are settling due to gravity and thermophoresis. The gravitational force acting on a particle is directly proportional to its mass, and can be expressed as follows

$$F_G = \left(\frac{\pi \rho_P}{6}\right) d_p^3 g \quad [5]$$

where ρ_p is the particle density and g is the gravitational constant. This force can be used to derive an expression for the moment settling velocity due to gravity. The moment thermophoretic velocity in the free-molecular limit is derived from the following force on a particle

$$F_{\text{thermo}} = \frac{-P\lambda d_p^2 \nabla T_g}{T_g} \quad [6]$$

where P is the reactor pressure, λ is the mean free path of the gas molecules, and T_g is the gas temperature. This expression for thermophoretic force assumes that the particles are smaller than the mean free path of the carrier gas. The results of the simulations will be seen to justify the use of this equation. The moment diffusion coefficient, Γ_k, is derived from the following particle diffusion coefficient

$$D_P = \frac{k_B T_g(1 + 1.43Kn^{1.049})}{3\pi\mu d_P} \quad [7]$$

where k_B is the Boltzmann constant, Kn is the Knudsen number (mean free path of the gas molecules divided by the particle radius), and μ is the gas viscosity.

The moment source term, S_k, in the governing equation presents the greatest difficulty for modeling because it consists of three processes, coagulation, condensation, and nucleation. Each of these processes affects the moments of the basis set differently based on the physical interpretation of each moment. The selection of the basis set of moments was partially motivated by the fact that the evaluation of the complex coagulation integrals could be avoided. Coagulation is a particle growth process in which two particles collide to form a larger particle. If the total particle volume is conserved through the interaction, coagulation will have a profoundly different impact on each of the moments in the basis set. Since the zeroth moment represents the particle number concentration, this quantity will decrease due to the coagulation process because the number of particles is reduced with each particle-particle collision. Indeed, the interpolation formula which represents the effect of coagulation on the zeroth moment is negative, and is given as follows[40,41]

$$S_{0\text{Coagulation}} = -4.8990\left[\frac{k_B T_g}{\rho_p}\right]^{1/2} M_0^{31/16} M_3^{-1/24} M_6^{5/48} \quad [8]$$

However, total particle volume is assumed to be conserved in collisions between particles, so the third moment which represents the particle volume fraction remains unchanged

$$S_{3\text{Coagulation}} = 0 \quad [9]$$

The sixth moment represents the efficiency with which the particles scatter light. In general, the larger the particle the greater its ability to scatter light. Prior research[40,41] has demonstrated that the interpolation formula for the effect of coagulation on the sixth moment is positive and is given as follows

$$S_{6\text{Coagulation}} = 2.6862\left[\frac{k_B T_g}{\rho_p}\right]^{1/2} M_0^{5/48} M_3^{13/8} M_6^{13/48} \quad [10]$$

Condensation is a particle growth process in which the surface of an existing particle serves as an interface upon which heterogeneous chemical reactions occur. The condensation source term is derived from the following equation for the volume growth rate of a particle[39]

$$\frac{dv_p}{dt} = \frac{\alpha P_s \pi d_p^2 v_m}{(2\pi m k_B T_g)^{1/2}} \quad [11]$$

where v_p is the particle volume, t is time, P_s is the partial pressure of the condensable species, α and m are the GCP (usually $\ll 1$) and mass of the condensable species molecules, and v_m is the molecular volume of the condensed phase. The growth of particles due to condensation is different from coagulation in that both a particle and a gaseous condensable species are involved. Growth of particles through condensation therefore involves two-way coupling between the chemistry and the aerosol model. When condensation occurs, the particles act as a sink for gas-phase condensable species and therefore perturb the gas-phase chemistry. An iterative procedure is therefore required to obtain both the flow/chemistry and aerosol solutions. The GCP, α, modifies the rate at which condensation occurs, where $0 < \alpha < 1$. In general, it becomes more difficult to iterate between the flow/chemistry and aerosol solutions as the value of the GCP increases. The present model was found to be very sensitive to the value of α, and thus the effects of condensation. Additionally, it was found that the GCP had to be adjusted in order to maintain agreement between the numerical and experimental results. This semiempirical approach is discussed further in the Results and Discussion portion of this paper.

Particle nucleation is a process in which a new particle is created from a collection of gas-phase molecules. Because these particles are new to the system and have yet to undergo any growth via condensation or coagulation, they are the smallest particles considered by the aerosol model. The addition of these particles, called monomers, significantly increases the particle number concentration. The monomer production rate, R_m, is computed by the gas-phase

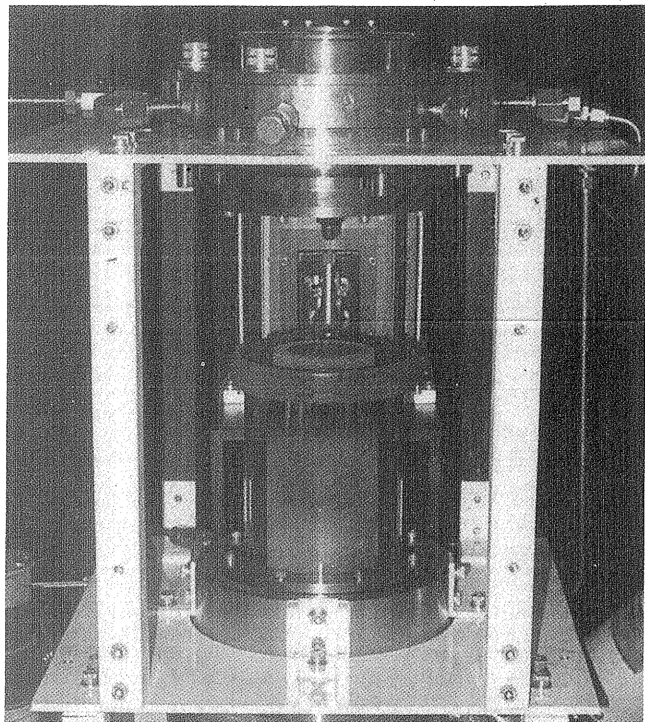

Figure 3. Photograph of the experimental rotating disk CVD reactor.

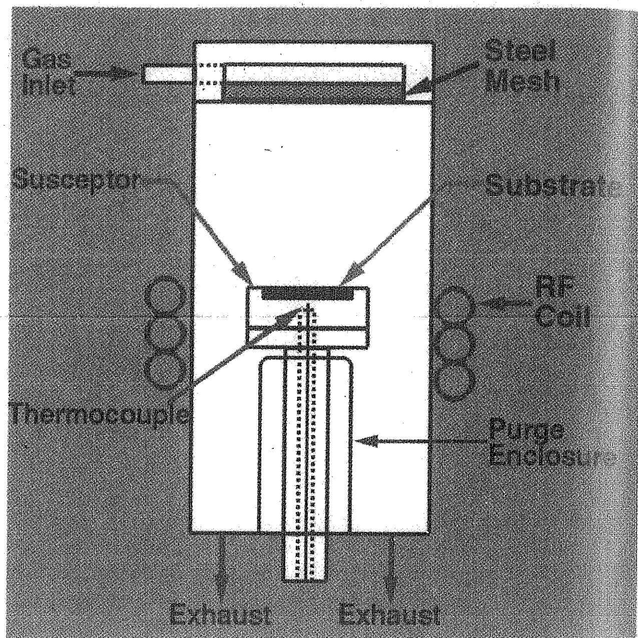

Figure 4. Schematic of the experimental rotating disk CVD reactor.

kinetic model as the rate of formation of the largest explicitly considered silicon cluster (see the description of the gas-phase chemistry for details). The effect of nucleation on the zeroth moment is represented as

$$S_{0\text{Nucleation}} = R_{\text{m}} \qquad [12]$$

Similar formulas are derivable for the remaining two moments of the basis set, both of which increase proportionally with the monomer production rate.

When the expressions for particle growth and transport are substituted into the governing differential equation, Eq. 4, the result is a highly nonlinear set of coupled differential equations which are solved using the LSODE solution package.[43] The resulting iteration involving the aerosol solution coupled with the flow/chemistry solver is carried out on high-performance workstations. The boundary conditions for the aerosol solution are that all moments are zero both at the surface of the susceptor and the inlet of the reactor. The results of the computation can be plotted as a function of the axial position above the susceptor. Values of M_6 can be compared with experimentally generated light-scattering intensity profiles. The accuracy of the aerosol model was verified through the solution of two model problems as outlined by Davis and Moore.[44]

Experimental

CVD reactor apparatus.—A photograph of the CVD reactor is shown in Fig. 3 and a schematic is shown in Fig. 4. This reactor is based on a previously reported design.[19,45-47] The process gases are injected at the top, flow through a stainless steel mesh into the 10 cm internal diameter quartz tube, and are exhausted through the bottom of the reactor. A 5.0 cm diam silicon substrate rests in the recess of a 6.7 cm diam molybdenum susceptor that is inductively heated with a 5 kW rf power supply. The distance from the mesh to the susceptor is 15 cm. A Chromel-Alumel thermocouple in contact with the susceptor base is used in the control of the rf power supply output to maintain the susceptor temperature. The nominal thermocouple temperature was 1100 K. The two gas compositions (by volume) employed were 10 mol % fraction nitrogen in a balance of helium or 0.25 mol % fraction silane in a balance of helium, hereafter referred to as mixture A and mixture B, respectively. All gases were purified with bulk gas purifiers prior to injection into the reactor. The nominal total gas flow rate was 19 L/min. All gas delivery lines were constructed of electropolished stainless steel tubing. Particle filters were located at the reactor gas entry port. The nominal chamber pressure was 26.7 kPa (200 Torr) as measured with a capacitance manometer. Nominal susceptor rotation rates were 500 and 1000 rpm. The reactor was mounted on a translation stage with three orthogonal axes of travel so that spatial profiles of gas temperature could be measured.

Gas-phase Raman spectroscopy.—Gas-phase temperatures were determined from the nitrogen rotational Raman spectra in gas mixture A. All temperatures reported here were recorded along the reactor centerline. Raman scattering was excited with 488 nm radiation from an argon ion laser with a laser power of *ca.* 5 W at the reactor. A holographic laser bandpass filter was used to remove laser plasma lines. The beam was focused into the reactor with a 500 mm focal length spherical lens that produced a beam waist with a *ca.* 250 μm diam. Scattered radiation was collected 90° to the direction of propagation of the exciting laser beam and collimated with a 50 mm diam, 200 mm focal length achromatic lens located at infinite conjugate ratio. A periscope, 488 nm holographic notch filter (150 cm^{-1} nominal spectral edgewidth and 6.0 nominal optical density) and a bandpass filter were placed in the collected, collimated radiation. The periscope consisted of two mirrors that served to rotate the image of the laser line so that the long axis of the image was parallel to the spectrograph slits. The bandpass filter was necessary to limit the amount of blackbody radiation entering the spectrograph so as to reduce interference from reentrant light. The filter was optimized for the *ca.* 450 to 558.5 nm wavelength range and possessed a nominal optical density of 5 from 558.5 to 1000 nm. A 50 mm diam, 350 mm focal length achromatic lens was used to couple radiation into a 0.5 m focal length, f/6.5 aperture ratio imaging spectrograph equipped with a 2400 groove/mm holographic grating, and optimized for use from 450 to 750 nm. A 2048 × 512 pixel array, back-illuminated, thermoelectrically cooled, charge coupled device (CCD) camera system was employed. The individual CCD pixel size was 13.5 × 13.5 μm. The sampling length in the reactor

was *ca.* 500 μm (65 rows of the CCD array were used). The instrumental bandpass (fwhm) was *ca.* 2 cm^{-1}. All spectra were obtained in integration times of 5 min or less.

Raman intensities were corrected for the wavelength-dependent response of the optical system[48] and by the factor of the square of the wavelength that is required in the transformation of the spectrum abscissa from the measured wavelength (in nanometers) to Raman shift expressed in wavenumber (cm^{-1}).[49] The intensity correction was performed by illuminating a reflecting surface placed at the focal point of the collection lens with a white light source of known relative irradiance. The white light source was a 15.2 cm diam Spectralon integrating sphere (Labsphere) that was equipped with a 10 W halogen bulb. Under the conditions employed in this work, the nitrogen natural lineshape is narrow (contributes less than 1% to the observed width) and the observed lineshape is determined primarily by the instrument function. The lineshape is well characterized for all rotational lines by fitting the low-frequency and the high-frequency sides to fifth and sixth order polynomials, respectively. A measured Raman spectrum was compared to a calculated spectrum, and a global search minimization was employed to minimize the sum of the residuals squared. The calculated spectrum was the convolution of the rotational Raman spectrum and the fit lineshape function, and was obtained using the Sandia CARS code modified for spontaneous Raman scattering.[50] This global fit to all rotational lines simultaneously is particularly useful to minimize the effects of noise on the spectrum, *e.g.*, rf interference, as well as to account for Raman scattering from excited vibrational states which becomes significant at *ca.* 1000 K and higher for nitrogen. Due to the sharp temperature gradients present in this reactor and pending the results of a separate investigation in a reference isothermal gas cell, a thorough error analysis has yet to be performed. Therefore, reported rotational temperatures must be considered tentative.

Elastic light scattering.—All elastic light scattering measurements were performed using gas mixture B, as detailed above. For these measurements a laser sheet was formed by expanding a 488 nm wavelength beam with a -25 mm focal length cylindrical lens and focusing the light with a 500 mm focal length cylindrical lens. The incident radiation was polarized parallel to the plane of the laser sheet. No polarization analysis of the scattered radiation was performed. At the susceptor center, the sheet was approximately 100 mm high (maximum optical access) with a width of approximately 250 μm. All scattering intensity measurements reported here were recorded along the reactor centerline. A 488 nm interference filter (3.1 nm nominal fwhm) was used to reject blackbody radiation. The scattered light was collected with an imaging lens oriented at 90° to the direction of propagation of the laser sheet. The same CCD camera used for Raman spectroscopy was used for elastic light scattering. With the magnification employed, the spatial resolution of the optical system was nominally 33 pixels/mm (as determined by a resolution test pattern). Ten columns of the CCD array (*ca.* 250 μm) were summed, and the nominal average intensity is presented here. All images were obtained in integration times of 4 s or less.

Results and Discussion

A fundamental understanding of many features critical to the CVD process, such as gas-phase chemical reactions, gas properties, and velocity profiles, begins with an accurate description of gas temperature. Figure 5 presents a comparison between the temperature profiles generated numerically using both the axisymmetric and 1-D SPIN models and the temperature profiles measured experimentally. Results are presented for susceptor rotation rates of 500 and 1000 rpm; for both cases the total reactor pressure was 26.7 kPa (200 Torr), the thermocouple was set to 1100 K, the axial velocity at the inlet was computed, using a flow rate of 19 L/min and the dimensions of the experimental reactor, to be 22 cm/s, and the inlet gas composition was 10 mol % N_2 in He. Nitrogen was included in the carrier gas due to the experimental technique employed to measure the gas temperature (see the description of the experiment for details). The surface temperature of the substrate was deduced by performing a linear regression fit to the experimental data collected near the substrate surface. The results of the regression indicated that for both cases there is a small temperature deviation between the exposed substrate surface and the thermocouple which is embedded within the susceptor. This deviation is largely due to convective heat transfer, and decreases with susceptor rotation rate. The substrate surface temperatures found through regression were assigned as boundary conditions for the numerical simulations.

The results of the numerical simulations indicate that the axisymmetric model is capable of accurately replicating the experimental temperature profiles for both rotation rates. However, the 1-D SPIN code was unable to simulate the experimental temperature profile for either rotation rate. Prior research[14] has demonstrated that the infi-

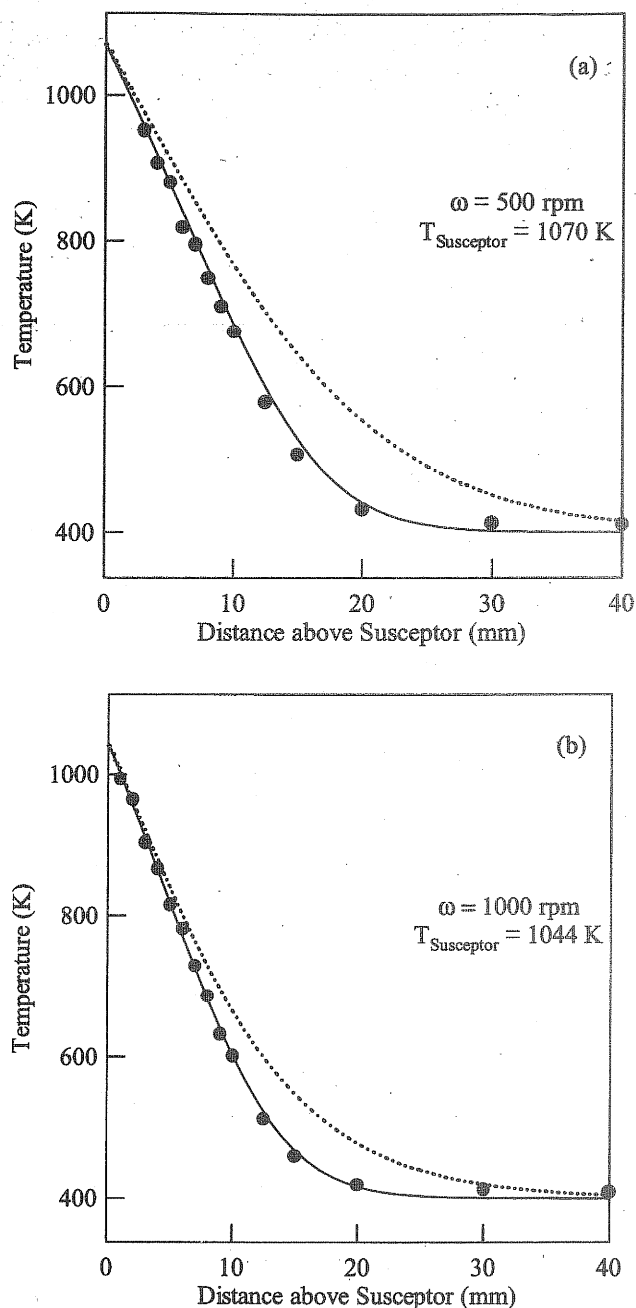

Figure 5. Gas-phase temperature profiles. (——) Axisymmetric model, (· · · ·) 1-D SPIN model, (●) experimental measurements. (a) ω = 500 rpm, $T_{susceptor}$ = 1070 K. (b) ω = 1000 rpm, $T_{susceptor}$ = 1044 K.

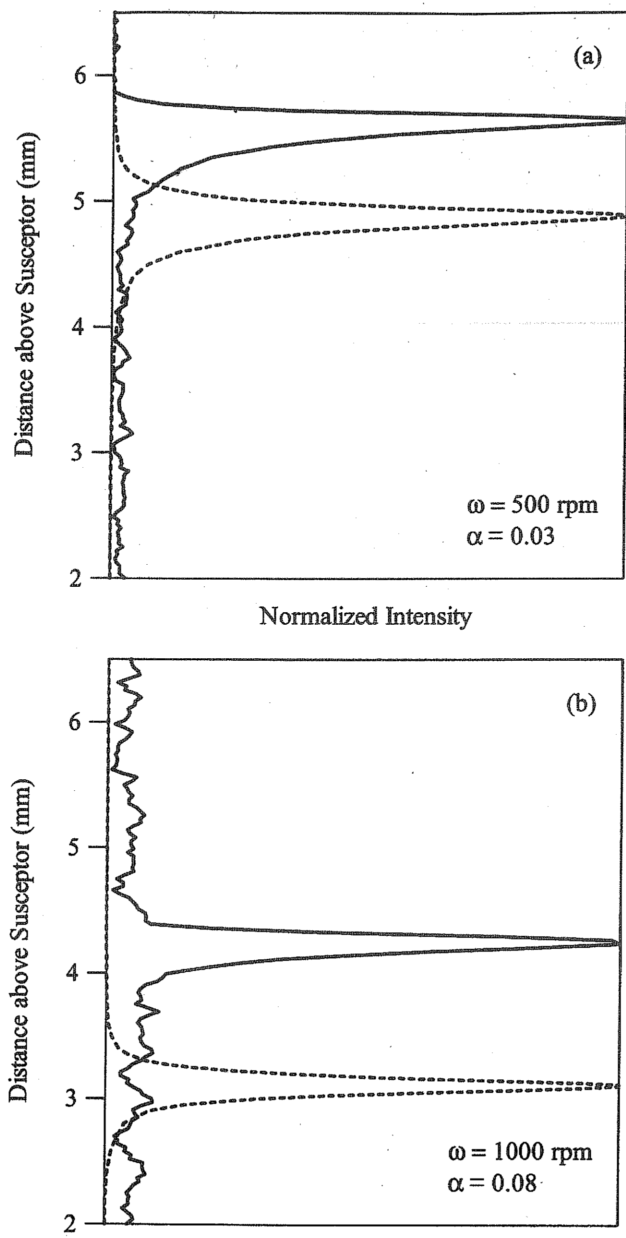

Figure 6. Normalized particle light scattering profiles. (——) Experimental profile, (· · · ·) numerical profile. (a) ω = 500 rpm, α = 0.03; (b) ω = 1000 rpm, α = 0.08.

nite disk assumption employed by the 1-D SPIN code is only accurate under conditions in which the boundary layer thickness is small in relation to the finite susceptor radius. This behavior is evident in the two cases considered in Fig. 5. The boundary layer thickness in the reactor varies as $(\omega P)^{-1/2}$, where ω is the susceptor rotation rate and P is the total reactor pressure, and indeed the agreement between the 1-D SPIN and experimentally measured temperature profiles does improve as the rotation rate increases. However, the significant deviation between the 1-D SPIN and experimentally measured profiles persists even at high rotation rates, so centerline temperature profiles taken from the axisymmetric model are used to draw comparisons with experimental data in an attempt to increase the validity of the simulations.

Figure 6 presents a comparison between experimentally measured particle light scattering intensity and the sixth moment computed by the 1-D aerosol model. Both profiles have been independently normalized to facilitate qualitative comparison. Experimental light scattering intensity profiles have been measured for susceptor rotation rates of 500 and 1000 rpm; for both cases the total reactor pressure was 26.7 kPa (200 Torr), the thermocouple was set to 1100 K, the inlet axial velocity was 22 cm/s, and the inlet gas composition was 0.25 mol % SiH_4 in helium. Prior measurements using similar reactor operating conditions have indicated that the surface temperature of the substrate is slightly lower than the thermocouple temperature. To account for this slight deviation, axisymmetric computations for both susceptor rotation rates were performed using a substrate surface temperature of 1075 K. For the reasons discussed previously, the gas-phase temperature profiles generated by the axisymmetric model were used by the 1-D SPIN/aerosol model. Several interesting conclusions can be drawn from Fig. 6. Recall that the accuracy of the infinite radius assumption in the 1-D SPIN model increases with susceptor rotation rate, yet the deviation in the light scattering profile increases at higher rotation rates. This behavior suggests that numerical errors associated with this assumption are not the primary cause of the light scattering profile deviation. A more likely explanation for the deviation is a physical process whose effect is not accounted for in the aerosol model, such as radiative heating of the particles. Additional work is necessary to elucidate the cause of this deviation between the experimental and numerical light scattering intensity profiles.

Another interesting aspect of Fig. 6 is that the value of the GCP, α, in the 1-D aerosol model controls the width of the sixth moment profiles. The GCP is a somewhat ambiguous quantity whose value depends on both the reactivity of condensable species and reactor operating conditions. The function of the GCP in this model is to regulate the rate of particle growth due to condensation via a spatially invariant multiplier, as detailed in Eq. 11. The value of the GCP for the numerical simulations was small (<0.1) and varied slightly with susceptor rotation rate. There are several plausible explanations for the sensitivity of the aerosol model to the rate of condensational growth. The 1-D aerosol model utilized here accounts for condensation via only one condensable species, which is likely an oversimplification of the actual physical process. Additionally, the GCP was invariant throughout the flow domain, which may not be correct in a reactor of this type which is characterized by large temperature and species concentration gradients near the susceptor surface. Regardless, the chosen values of α produce very good agreement between the shapes of the experimental light scattering intensity profiles and the numerical sixth moment profiles.

Additional details about the aerosol populations which arise under the reactor operating conditions detailed in Fig. 6 are presented in Fig. 7. Note that the scaling of the abscissas in Fig. 7 is not consistent. Using the information presented in Fig. 7, it is possible to make generalizations about the behavior of the aerosol populations for rotation rates of 500 (Fig. 7a) and 1000 (Fig. 7b) rpm. For both rotation rates there is a discontinuity in the shape of the particle number concentration profile. The location of this discontinuity, in both cases, coincides with the location of both the sixth moment (see Fig. 6) and average particle diameter maxima. Based on the current 1-D aerosol model, there can be only one plausible explanation for this behavior. Recall that only two source terms in the aerosol model affect the particle number concentration, coagulation and nucleation. It is not possible for nucleation alone to cause the change in inflection observed in the number concentration profile of Fig. 7a. Therefore, the rate of coagulation must increase at the location of the discontinuity, an effect which would produce both larger and fewer particles. Evidence to support this assertion can be seen in the average particle diameter profiles on the right of each plot in Fig. 7. An increase in the rate of coagulation would partially explain the maxima in the average particle size at the same axial location as the aforementioned discontinuity. However, consideration of coagulation alone is not sufficient to explain the behavior of the average particle diameter profiles. Recall that the rate of particle growth due to condensation was proportional to the diameter of the particle. Therefore as the size of particles increases due to coagulation, the

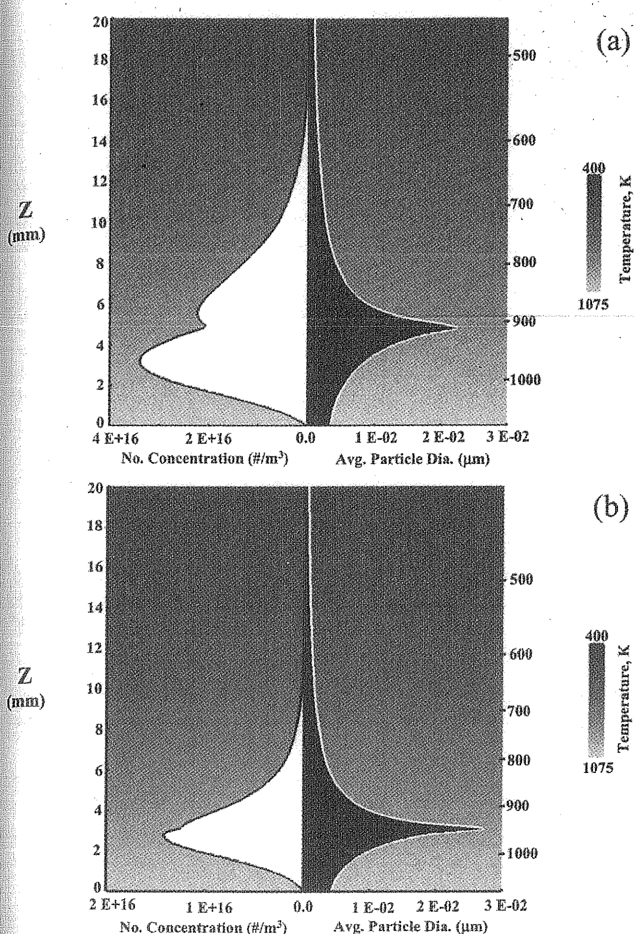

Figure 7. Particle population characteristics: at left, number concentration, at right, average particle diameter. (a) $\omega = 500$ rpm, $\alpha = 0.03$. (b) $\omega = 1000$ rpm, $\alpha = 0.08$.

rate of condensation also increases, a phenomena which results in the large increase in average particle diameter at the discontinuity location. Simulations in which the condensation source term is ignored, or the rate of coagulation is relaxed, did not produce aerosol populations with the characteristics observed in Fig. 6 and 7. These aforementioned cases did not result in a clear sixth moment maxima, a discontinuity in the number concentration profile, or a maximum in the average particle diameter profile. The steep gradients which are characteristic for this type of reactor imply that the gas-phase decomposition of the silicon precursor and the growth of the aerosol population are confined within the narrow thermal boundary layer. This unique set of conditions thus leads to aerosol populations whose behavior is also characterized by abrupt gradient changes.

In addition to the general behavior of the profiles presented in Fig. 7, there are some specific differences between the two plots that can be attributed directly to the rotation rate. For the reasons discussed earlier, increasing the rotation rate reduces the thickness of both the velocity and thermal boundary layers. This behavior is evidenced in Fig. 7 by the fact that the maxima in both the number concentration and average particle diameter profiles has moved closer to the susceptor surface at increased susceptor rotation rates. Also, the thicker thermal boundary layer and longer residence time at lower susceptor rotation rates combine to produce over twice as many particles as are present at higher rotation rates. Interestingly, there is little variation in the average particle diameter as the rotation rate varies. The rate of susceptor rotation is only one variable which affects the aerosol population within the reactor.

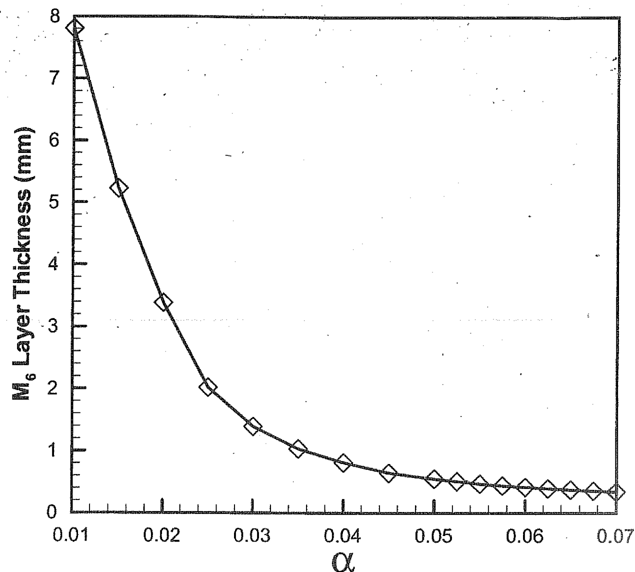

Figure 8. Sixth moment profile thickness *vs.* GCP, α. $T_{susceptor} = 1075$ K, $P_{total} = 26.7$ kPa (200 Torr), $\omega = 1000$ rpm, 0.25% SiH_4 in helium, and $U_\infty = 22$ cm/s.

The sensitivity of the sixth moment profile to the value of the GCP is shown in Fig. 8. Simulations were performed using various values of the GCP, where the substrate temperature was 1075 K, the total reactor pressure was 26.7 kPa (200 Torr), the inlet axial velocity was 22 cm/s, the inlet gas composition was 0.25 mol % SiH_4 in helium, and the susceptor rotation rate was 1000 rpm. At smaller values of the GCP, the width of the sixth moment profile was very broad, in some cases so broad as to lack a clear maxima. As the

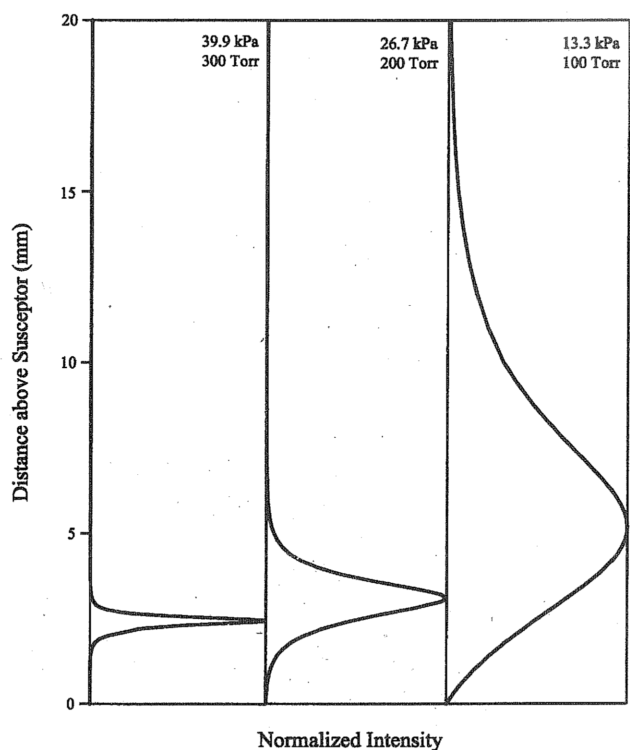

Figure 9. Sixth moment profile *vs.* total reactor pressure. $T_{susceptor} = 1075$ K, $\alpha = 0.02$, $\omega = 1000$ rpm, 0.25% SiH_4 in helium, and $U_\infty = 22$ cm/s.

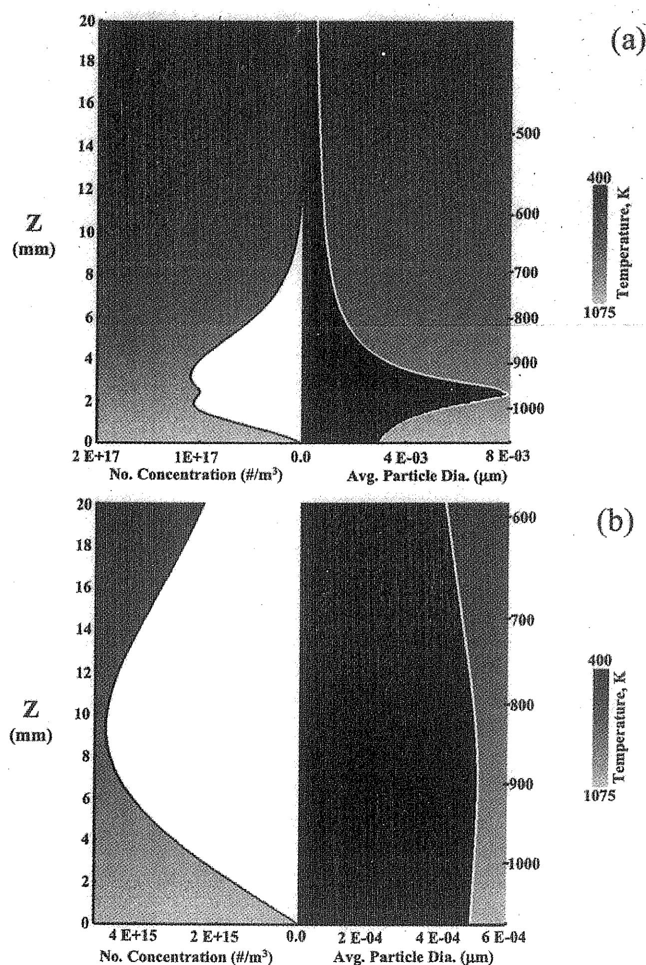

Figure 10. Particle population characteristics: at left, number concentration, at right, average particle diameter. (a) 39.9 kPa (300 Torr). (b) 13.3 kPa (100 Torr).

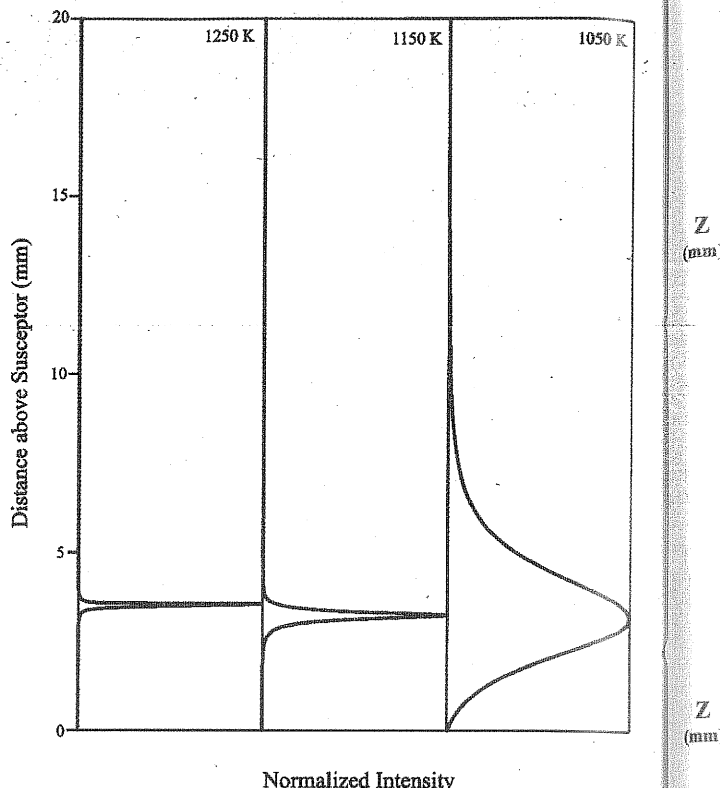

Figure 11. Sixth moment profile *vs.* $T_{susceptor}$. P_{total} = 26.7 kPa (200 Torr), α = 0.018, ω = 1000 rpm, 0.25% SiH_4 in helium, and U_∞ = 22 cm/s.

value of the GCP increases, the rate of particle growth due to condensation also increases, which results in a rapid decrease in the thickness of the sixth moment profile. At larger values of the GCP, there is a nearly linear relationship between the thickness of the sixth moment profile and the value of GCP. Simulation becomes more difficult at higher values of the GCP because additional grid points are necessary to resolve the abrupt gradient changes which are characteristic of the sixth moment profile. It was difficult to predict *a priori* the location or quantity of the additional grid points based on the reactor operating conditions and the value of the GCP. For these reasons an adaptive grid refinement algorithm was incorporated into the 1-D aerosol model. For reactor operating conditions considered in this work, the characteristics of the aerosol population were very sensitive to the value of GCP.

Sixth moment profiles for various values of total reactor pressure are shown in Fig. 9. Simulations were performed with a substrate temperature of 1075 K, an inlet axial velocity of 22 cm/s, a GCP of 2.0×10^{-2}, a susceptor rotation rate of 1000 rpm, and an inlet gas composition of 0.25 mol % SiH_4 in helium. The value of the GCP was chosen to facilitate simulation at elevated total reactor pressures. Two interesting conclusions can be drawn from Fig. 9. As the total reactor pressure decreases the height of the sixth moment maxima relative to the susceptor surface increases. Additionally, the thickness of the sixth moment profile broadens as the total reactor pressure decreases. The behavior demonstrated by the sixth moment profile implies that multiple physical processes occurring within the reactor are sensitive to the total reactor pressure. Prior research has established that both the flow field and heat transfer are affected by the total reactor pressure.[14] As noted previously, the thickness of the boundary layer decreases as $(P)^{-1/2}$. Therefore, changes in the location of the sixth moment maxima with total reactor pressure can be attributed to changes in the flow field. The change in the thickness of the sixth moment profile has more subtle implications. As the total reactor pressure decreases, the partial pressure of the silicon precursor at the reactor inlet decreases. Therefore, the partial pressure of the condensable species decreases and, since the value of the GCP is invariant for these simulations, the rate of condensation ultimately decreases. The effect of reducing the rate of particle growth due to condensation is that the thickness of the sixth moment profile increases. Furthermore, as the total reactor pressure decreases the rate of particle diffusion increases. This increase in particle diffusion does contribute to the broadening of the sixth moment profile as observed in Fig. 9. Additional details relating to the characteristics of the aerosol population at various pressures can be found in Fig. 10.

Figure 10 presents details of the particle population for two values of the total reactor pressure, 39.9 kPa (300 Torr) and 13.3 kPa (100 Torr), for the reactor operating conditions detailed in Fig. 9. Note that the scaling of the abscissas in Fig. 10 is not consistent. Several interesting observations are possible based on the information contained in Fig. 10. At lower pressures (see Fig. 10b) the thickness of the thermal boundary layer increases substantially, as evidenced by the temperature ordinate on the right side of each plot. However, the increased thickness of the thermal boundary layer at lower pressure does not result in an increased number of particles. The results illustrated in Fig. 10 indicate that the particle number concentration at reduced reactor pressure (Fig. 10b) was approximately two orders of magnitude lower than the higher pressure case (Fig. 10a). However, for the higher pressure case the growth of large numbers of particles was confined to a narrow region near the surface of the susceptor. Additionally, the characteristics of the average

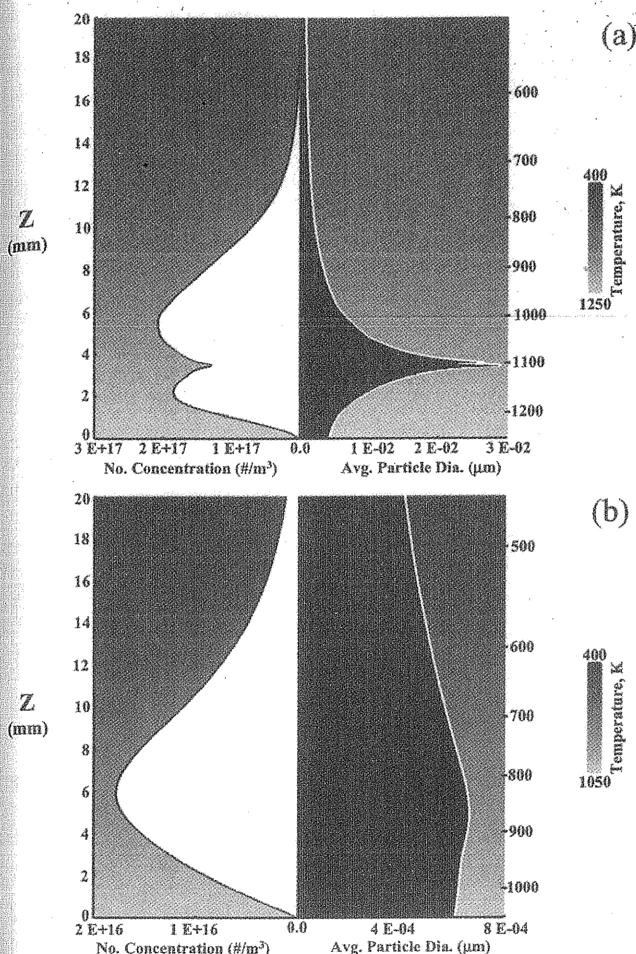

Figure 12. Particle population characteristics: at left, number concentration, at right, average particle diameter. (a) $T_{susceptor} = 1250$ K. (b) $T_{susceptor} = 1050$ K.

particle diameter profiles differ substantially with pressure. For the lower pressure simulation (Fig. 10b) the average particle diameter profile lacks a clearly defined maxima, and the results of the simulation indicate that the average particle diameter is more than an order of magnitude smaller when compared with the higher pressure results. These results demonstrate that the particles are less numerous and grow more slowly at lower total reactor pressures.

The sensivity of the sixth moment profile to substrate temperature is presented in Fig. 11. Simulations were performed with a total reactor pressure of 26.7 kPa (200 Torr), an inlet axial velocity of 22 cm/s, a GCP of 1.8×10^{-2}, a susceptor rotation rate of 1000 rpm, and an inlet gas composition of 0.25 mol % SiH_4 in helium. The value of the GCP was chosen to facilitate simulation at elevated substrate temperature. As the substrate temperature decreases the thickness of the sixth moment profile increases. Additionally, as the substrate temperature increases the height of the sixth moment maxima relative to the substrate surface increases. The behavior demonstrated by the sixth moment profile indicates that multiple physical processes are affected by the change in the substrate temperature. However, unlike the pressure-dependent simulations detailed in Fig. 9, the characteristics of the flow field are not altered significantly by changes in the substrate temperature. Therefore, the change in the location of the sixth moment maximum with substrate temperature cannot be attributed solely to changes in the flow field; a more likely explanation would be thermophoresis. Recall, that thermophoresis is a temperature-dependent force which drives a particle away from a hot region in the presence of a thermal gradient.

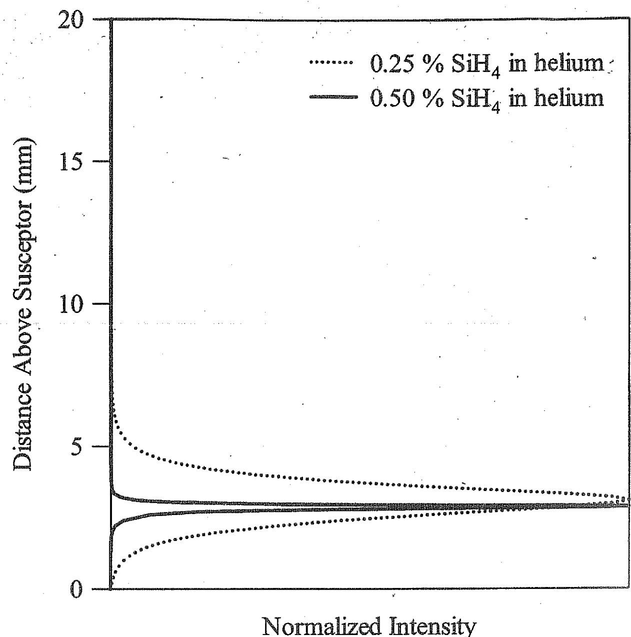

Figure 13. Sixth moment profile *vs.* SiH_4 inlet concentration. (· · · ·) 0.25% SiH_4 in helium, (——) 0.50% SiH_4 in helium. $T_{susceptor} = 1075$ K, $P_{total} = 26.7$ kPa (200 Torr), $\alpha = 0.02$, $\omega = 1000$ rpm, and $U_\infty = 22$ cm/s.

Increasing the substrate temperature would increase the thermophoretic force acting on the particles, thus increasing the layer height. An explanation for the change in the shape of the sixth moment profile with substrate temperature lies with gas-phase chemical reaction. As the temperature of the substrate decreases, less energy is available to drive the gas-phase reactions which produce both nucleated particles and condensable species. Therefore, at lower substrate temperatures the partial pressure of the condensable species decreases and, since the value of the GCP is invariant for these simulations, the rate of condensation ultimately decreases. The effect of reducing the rate of particle growth due to condensation is that the thickness of the sixth moment profile increases.

Figure 12 presents details of the particle populations for two values of the substrate temperature, 1250 K (Fig. 12a) and 1050 K (Fig. 12b), for the reactor operating conditions detailed in Fig. 11. Note that the scaling of the abscissas in Fig. 12 is not consistent. The information contained in Fig. 12 demonstrates the effect of condensation on the characteristics of the particle population. The average particle diameter profile for the higher temperature simulation has a distinct maxima at a location which coincides with both the sixth moment peak and a large discontinuity in the particle number concentration. For reasons discussed previously, this behavior implies that the rate of particle growth through condensation increases at this location. The characteristics of the particle population for the lower temperature simulation indicate that rapid particle growth due to condensation does not occur. Evidence to support this assertion can be seen in the average particle diameter plot in Fig 12b. The maximum average particle diameter for the lower temperature simulation was approximately two orders of magnitude smaller than the higher temperature results. Additionally, the average particle diameter profile for the lower temperature simulation lacked a clearly defined maxima which was clearly observed in the higher temperature simulation. As discussed previously, these results imply that the rate of particle growth due to condensation was reduced for the lower temperature simulation.

Figure 13 presents a comparison of sixth moment profiles for two values of the inlet gas composition, 0.50 and 0.25 mol % SiH_4 in helium. Simulations were performed with a total reactor pressure of

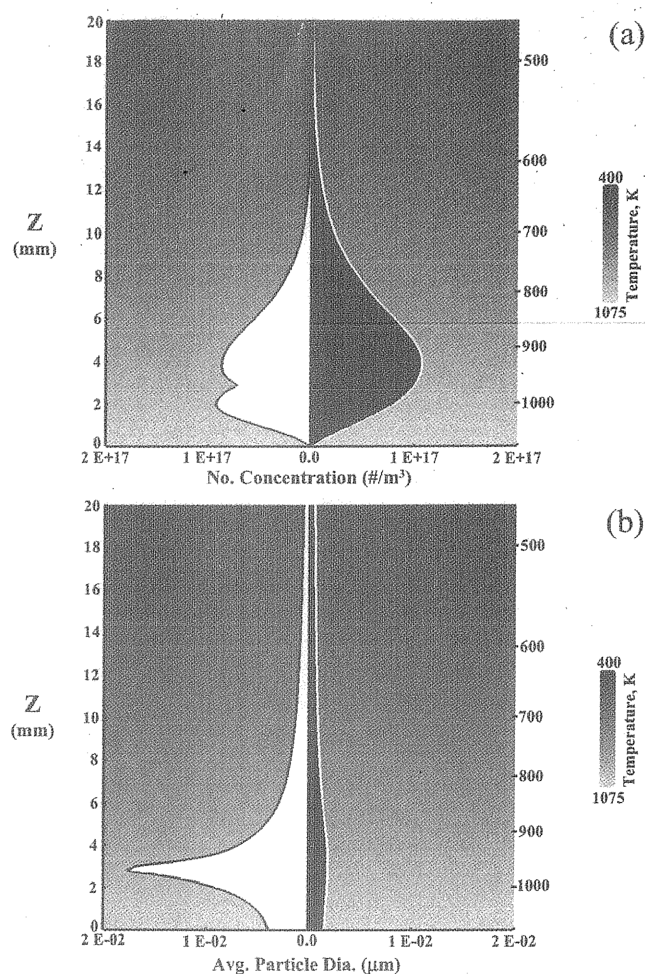

Figure 14. Particle population characteristics: at left, 0.50% SiH_4 in helium, at right, 0.25% SiH_4 in helium. (a) Number concentration, (b) average particle diameter.

26.7 kPa (200 Torr), a substrate temperature of 1075 K, an inlet axial velocity of 22 cm/s, a GCP of 2.0×10^{-2}, and a susceptor rotation rate of 1000 rpm. The value of the GCP was chosen to facilitate simulation at elevated SiH_4 concentration. Increasing the amount of SiH_4 in the inlet gas has little effect on the location of the sixth moment maxima. This implies that the flow field and heat transfer are controlled by the helium carrier gas, and the addition of small amounts of SiH_4 was not sufficient to alter the characteristics of either the flow field or heat transfer. However, as the concentration of SiH_4 increased, the thickness of the sixth moment peak decreased. This behavior can be attributed to the increased rate of particle growth due to condensation which occurs at increased SiH_4 concentrations. The increase in SiH_4 partial pressure at the reactor inlet results in an increase in the partial pressure of the condensable species due to the gas-phase reaction. Therefore, since the GCP is invariant for these simulations, the rate of condensation increases.

Characteristics of the particle populations for the conditions in Fig. 13 are detailed in Fig 14. Several interesting observations can be made based on the information contained in Fig. 14. Notice in Fig. 14a that increasing the SiH_4 concentration at the reactor inlet, at left, does not result in a larger number concentration of particles. This can be attributed to a depletion in the gas-phase partial pressure of silicon due to condensation. Recall that the condensable species was an intermediate molecule which arose during the gas-phase decomposition of SiH_4. Depletion of this intermediate through condensation results in larger particles and fewer condensable molecules able to decompose through gas-phase reaction. Evidence to support this assertion can be observed in Fig. 14b. Notice that the average particle diameter profile for the larger SiH_4 inlet concentration, at left, exhibits a clear maxima which has been attributed previously to rapid particle growth due to condensation. The resulting particles are much larger than the smaller SiH_4 case, at right, which indicates that condensation is more rapid for the case with the larger SiH_4 inlet concentration.

Conclusions

This work has demonstrated that during the epitaxial deposition of silicon from SiH_4 the gas-phase nucleation, growth, and transport of silicon particles is an active and important physical process. The characteristics of these particles were demonstrated to be very sensitive to reactor operating conditions. In many cases, alterations to the reactor operating conditions which have been shown previously to enhance the deposition rate[16] give rise to larger and more numerous particle populations. Trends observed in the particle populations suggest that increasing the total reactor pressure or substrate temperature can potentially result in larger numbers of particles forming in the gas phase. Additionally, increasing the rotation rate of the susceptor thins the thermal boundary layer, resulting in the particle layer moving closer to the substrate surface. Additional research is necessary to identify reactor operating conditions which can maximize the deposition rate and minimize particle formation and growth. This research has also demonstrated the importance of identifying reactive gas-phase intermediate species and incorporating condensation into both the gas-phase reaction mechanism and the aerosol model. It has been shown that properly accounting for particle growth via condensation profoundly alters the characteristics of the aerosol population in such a way as to allow for excellent agreement with experiment. Additional research is necessary, however, on the nature of the GCP, which has been treated in an obviously oversimplified manner in this paper. Finally, further development of aerosol models for reactors such as this is clearly dependent on the acquisition of additional reliable experimental data that can properly elucidate the underlying physics and chemistry.

Acknowledgments

The authors gratefully acknowledge Professor M. R. Zachariah of the Department of Mechanical Engineering, University of Minnesota, and Dr. C. A. Wang of Lincoln Laboratory, Massachusetts Institute of Technology, for helpful discussions. R. R. Fink of NIST assisted in the assembly and operation of the experimental CVD reactor.

Certain commercial equipment, instruments, and materials are identified in this publication to adequately specify the experimental procedure. Such identification in no way implies approval, recommendation, or endorsement by the National Institute of Standards and Technology, nor does it imply that the equipment, instruments, or materials identified are necessarily the best available for the purpose.

National Institute of Standards and Technology assisted in meeting the publication costs of this article.

References

1. C. R. Kleijn, K. J. Kuijlaars, M. Okkerse, H. van Santen, and H. E. A. van den Akker, *J. Phys. IV*, **9**, 117 (1999).
2. J. M. Jasinski, B. S. Meyerson, and B. A. Scott, *Annu. Rev. Phys. Chem.*, 38, 109 (1987).
3. P. Ho, M. E. Coltrin, and W. G. Breiland, *J. Phys. Chem.*, **98**, 10138 (1994).
4. J. H. Purnell and R. Walsh, *Proc. R. Soc. London, Ser. A*, **293**, 543 (1966).
5. C. G. Newman, H. E. O'Neal, M. A. Ring, F. Leska, and N. Shipley, *Int. J. Chem. Kinet.*, **11**, 1167 (1979).
6. M. E. Coltrin, R. J. Kee, and J. A. Miller, *J. Electrochem. Soc.*, **131**, 425 (1984).
7. F. C. Eversteijn, *Philips Res. Rep.*, **26**, 134 (1971).
8. M. T. Swihart and S. L. Girshick, *J. Phys. Chem. B*, **103**, 64 (1999).
9. G. H. Evans and R. Greif, *J. Heat Transfer*, **109**, 928 (1987).
10. K. F. Jensen, E. O. Einset, and D. I. Fotiadis, *Annu. Rev. Fluid Mech.*, 23, 197 (1991).
11. H. Moffat and K. F. Jensen, *J. Cryst. Growth*, **77**, 108 (1986).

12. D. I. Fotiadis, A. M. Kremer, D. R. McKenna, and K. F. Jensen, *J. Cryst. Growth*, **85**, 154 (1987).
13. G. H. Evans and R. Greif, *Numer. Heat Transfer*, **12**, 243 (1987).
14. W. G. Breiland and G. H. Evans, *J. Electrochem. Soc.*, **138**, 1806 (1991).
15. R. W. Davis, E. F. Moore, and M. R. Zachariah, *J. Cryst. Growth*, **132**, 513 (1993).
16. M. E. Coltrin, R. J. Kee, and G. H. Evans, *J. Electrochem. Soc.*, **136**, 819 (1989).
17. M. E. Coltrin, R. J. Kee, and J. A. Miller, *J. Electrochem. Soc.*, **133**, 1207 (1986).
18. R. Pollard and J. Newman, *J. Electrochem. Soc.*, **127**, 744 (1980).
19. S. Patnaik, R. A. Brown, and C. A. Wang, *J. Cryst. Growth*, **96**, 153 (1989).
20. E. R. Whitby and M. Hoshino, *J. Electrochem. Soc.*, **143**, 3397 (1996).
21. S. L. Girshick, M. T. Swihart, S. M. Suh, M. R. Mahajan, and S. Nijhawan, *J. Electrochem. Soc.*, **147**, 2303 (2000).
22. E. R. Whitby, P. H. McMurry, U. Shankar, and F. S. Binkowski, U.S. Environmental Protection Agency Report Number 68-01-7365, Research Triangle Park, NC (1991).
23. M. E. Coltrin, R. J. Kee, G. H. Evans, E. Meeks, F. M. Rupley, and J. F. Grcar, Sandia National Laboratories Report SAND91-8003, Albuquerque, NM (1991).
24. R. J. Kee, F. M. Rupley, and J. A. Miller, Sandia National Laboratories Report SAND89-8009, Albuquerque, NM (1989).
25. M. E. Coltrin, R. J. Kee, and F. M. Rupley, Sandia National Laboratories Report SAND90-8003B, Albuquerque, NM (1991).
26. R. J. Kee, G. Dixon-Lewis, J. Warnatz, M. E. Coltrin, and J. A. Miller, Sandia National Laboratories Report SAND86-8246, Albuquerque, NM (1986).
27. T. Kim, S. M. Suh, S. L. Girshick, M. R. Zachariah, P. H. McMurry, R. M. Rassel, Z. Shen, and S. A. Campbell, *J. Vac. Sci. Technol. A*, **20**, 413 (2002).
28. S. M. Suh, M. R. Zachariah, and S. L. Girshick, *J. Aerosol Sci.*, **33**, 943 (2002).
29. P. J. Zandbergen and D. Dijkstra, *Annu. Rev. Fluid Mech.*, **19**, 465 (1987).
30. H. J. Mick, P. Roth, V. N. Smirnov, and I. S. Zasionko, *Kinet. Katal.*, **35**, 439 (1994).
31. H. J. Mick, M. W. Markus, P. Roth, and V. N. Smirnov, *Ber. Bunsenges. Phys. Chem.*, **99**, 880 (1995).
32. D. L. Martin, L. M. Raff, and D. L. Thompson, *J. Chem. Phys.*, **92**, 425 (1990).
33. R. G. Gilbert, K. Luther, and J. Troe, *Ber. Bunsenges. Phys. Chem.*, **87**, 161 (1983).
34. W. G. Breiland, M. E. Coltrin, and P. Ho, *J. Appl. Phys.*, **59**, 3267 (1986).
35. A. A. Onischuk, V. P. Strunin, M. A. Ushakova, and V. N. Panfilov, *Int. J. Chem. Kinet.*, **30**, 99 (1998).
36. A. A. Onischuk, A. I. Levykin, V. P. Strunin, M. A. Ushakova, R. I. Samoilova, K. K. Sabelfeld, and V. N. Panfilov, *J. Aerosol Sci.*, **31**, 879 (2000).
37. C. Seigneur, A. B. Hudischewskyj, J. H. Seinfeld, K. T. Whitby, E. R. Whitby, J. R. Brock, and H. M. Barnes, *Aerosol. Sci. Technol.*, **5**, 205 (1986).
38. W. C. Hinds, *Aerosol Technology*, John Wiley & Sons Inc., New York (1982).
39. S. K. Friedlander, *Smoke, Dust and Haze*, John Wiley & Sons, New York (2000).
40. M. R. Zachariah and H. G. Semerjian, *AIChE J.*, **35**, 2003 (1989).
41. R. A. Dobbins and G. W. Mulholland, *Combust. Sci. Technol.*, **40**, 175 (1984).
42. C. T. Crowe, M. Sommerfeld, and Y. Tsuji, *Multiphase Flows with Droplets and Particles*, CRC Press, Boca Raton, FL (1998).
43. K. Radhakrishnan and A. C. Hindmarsh, Lawrence Livermore National Laboratory Report UCRL-ID-113855, Livermore, CA (1993).
44. R. W. Davis and E. F. Moore, *Aerosol. Sci. Technol.*, **31**, 456 (1999).
45. C. R. Biber, C. A. Wang, and S. Motaker, *J. Cryst. Growth*, **123**, 545 (1992).
46. J. E. Maslar, W. S. Hurst, D. M. Kremer, and S. H. Ehrman, in *Fundamental Gas-Phase and Surface Chemistry of Vapor Deposition II/Process Control, Diagnostics and Modeling in Semiconductor Manufacturing IV*, M. D. Allendorf, M. T. Swihart, and M. Meyyappan, Editors, PV 2001-13, p. 168, The Electrochemical Society Proceedings Series, Pennington, NJ (2001).
47. R. W. Davis, E. F. Moore, J. E. Maslar, D. R. Burgess, D. M. Kremer, and S. H. Ehrman, in *Proceedings of Characterization and Metrology for ULSI Technology: 2000 International Conference*, D. G. Seiler, A. C. Diebold, T. J. Shaffner, R. McDonald, W. M. Bullis, P. J. Smith, and E. M. Secula, Editors, p. 292, American Institute of Physics, New York (2001).
48. M. Fryling, C. J. Frank, and R. L. McCreery, *Appl. Spectrosc.*, **47**, 1965 (1993).
49. K. J. Frost and R. L. McCreery, *Appl. Spectrosc.*, **52**, 1614 (1998).
50. R. E. Palmer, Sandia National Laboratories Report SAND89-8206, Albuquerque, NM (1989).